

Composite Finite Elements for 3D Elasticity with Discontinuous Coefficients

Lars Ole Schwen*

Tobias Preusser[†]

Martin Rumpf*

For the numerical simulation in continuum mechanics the Composite Finite Element (CFE) method allows an effective treatment of problems in which material parameters are discontinuous across geometrically complicated interfaces. Instead of complicated and computationally expensive tetrahedral meshing, specialized CFE basis functions are constructed on a uniform hexahedral grid. This is a convenient approach in practice because frequently in biomechanics geometric interfaces are described via 3D image data given as voxel data on a regular grid. Then, for a particular coupling condition that depends on an underlying physical conservation law and the local geometry of the interface, one constructs CFE basis functions that are capable of representing functions satisfying this coupling condition. In this paper we present in detail this construction for heat conduction and linear elasticity as scalar and vector-valued model problems. Furthermore, we show first numerical results.

Keywords: Composite Finite Elements, heat diffusion, linear elasticity, jumping coefficients
AMS Subject Classifications (MSC2000): 74S05, 74B05, 65D05, 65M60, 65N30

1 Introduction

In many technical and medical applications physical processes on multi-phase materials with complicated interfaces have to be simulated. Let us mention a few examples. Technical applications include heat conduction in chip design [9] and the elastic behavior of composite materials, e.g. [23]. Some medical applications are the simulation of heat distribution during RF ablation therapy [15], electric fields in the human body as the forward problem of electrocardiography [12], the brain shift in neurosurgery [35], and effects of vertebroplasty on macroscopic properties of trabecular microstructure [14].

The standard FE procedure in this context is to generate a geometrically complicated simplicial (i.e. triangular or tetrahedral in 2D or 3D, respectively) FE mesh that represents the interface between the different materials and then use relatively simple FE basis functions for the discretization of the physical quantities. Good 3D meshing, however, is not a trivial task [2, 10, 28, 30, 29] and may require substantial user interaction. There are already various approaches available in the literature that avoid meshing, see [6, 1, 16, 8] for overviews on those “meshless methods”. In many applications, the geometric description of the objects considered is obtained by 3D imaging

*Institute for Numerical Simulation, University of Bonn ✉ Endenicher Allee 60, 53115 Bonn, Germany
{martin.rumpf,ole.schwen}@ins.uni-bonn.de

[†]Fraunhofer Institute for Medical Image Computing MEVIS; Jacobs University Bremen
tobias.preusser@mevis.fraunhofer.de

(MRI, CT, ...). Such voxel data inherently defines a uniform (topologically) hexahedral grid. Binary segmentation and assigning material properties (cf. [20, 33, 19, 31, 37, 5] for the case of material-void interfaces) suffers from a non-smooth interface representation. This can be remedied by subsequent smoothing of the mesh [3], at the possible cost of distorting elements.

As an alternative, the Composite Finite Element (CFE) [26, 17, 25, 24] method presented here uses a standard hexahedral grid and represents the geometric complexity of the interface via adapted basis functions. Given the geometry of an interface, material properties on both sides and a physical conservation law, one can derive local coupling conditions for the physical quantity under consideration, e.g. continuity along the interface and a discontinuous derivative across the interface. CFE basis functions are constructed such that they can suitably represent this behavior when applying a corresponding nodal interpolation on the standard hexahedral grid.

The overall construction of the adapted basis function is as follows. The hexahedral grid cells are first divided in six tetrahedra. These are further subdivided such that the interface is approximated via piecewise planar facets. This local construction is never stored but only temporarily generated to assemble the required finite element matrices. We refer here to [17] for the algorithmic description of this temporary subdivision process in the context of composite finite elements and to the classical marching cubes [18] and marching tetrahedra [32] algorithms for the overall algorithmic approach. In [17] composite finite elements are discussed in the case of complicated domain boundary represented as level sets of a given function on a hexahedral mesh, whereas in this paper we treat the case of complicated interior interfaces. Thus, based on this local and temporary grid, we present here the construction of a local linear interpolation scheme from neighboring nodes of the “regular” computational grid to additional nodes on the local, temporary grid obeying the local coupling condition. These interpolation weights are used to compose CFE basis functions as weighted sums of standard affine tent functions on the virtual grid—hence the term “composite”.

Outline of the article. The intention of this article is to provide a detailed discussion of coupling conditions and consequently the construction of CFE basis functions for two model problems: (scalar) heat conduction and (vector-valued) linear elasticity. In Section 2, we will discuss the construction for 2D isotropic heat conduction, already explaining all essential steps in the simpler scalar case. Furthermore we investigate how this can be extended to 3D and anisotropic material properties. The CFE construction for 2D Lamé-Navier elasticity and its extension to 3D and anisotropic linear elasticity is then presented in Section 3. Some algorithmic aspects assembling CFE matrices are discussed in Section 4. Finally, Section 5 shows first results obtained by the proposed CFE method.

2 Composite Finite Elements for Heat Diffusion

Let us first consider heat diffusion as a scalar model problem, with the corresponding elliptic operator

$$u \mapsto -\operatorname{div}(\mathcal{A}\nabla u) \tag{1}$$

on a domain Ω for \mathcal{A} being a second-order thermal diffusivity tensor and temperature u . We assume that the domain Ω is subdivided into two subdomains Ω_+ and Ω_- ($\Omega = \Omega_+ \cup \Omega_-$ and $\Omega_+ \cap \Omega_- = \emptyset$) with a piecewise smooth but geometrically complicated interface $\overline{\Omega_+} \cap \overline{\Omega_-}$. The diffusivity, represented by the diffusion tensor \mathcal{A} is now allowed to jump on the interface. In what follows we already assume that the interface is piecewise polygonal and consists of facets of simplices generated in the local subdivision step mentioned above.

2.1 Coupling Condition for Isotropic Heat Diffusion in 2D

At first we consider isotropic heat diffusion with corresponding operator

$$u \mapsto -\operatorname{div}(a\nabla u) \quad (2)$$

with a scalar thermal diffusivity coefficient a (i.e. $\mathcal{A} = a\mathbb{1}$ in Equation (1)). Energy conservation at the interface implies a continuous heat flux across (i.e. in normal direction N to) the interface

$$\langle a^+\nabla u^+, N \rangle = \langle a^-\nabla u^-, N \rangle \quad (3)$$

which translates to

$$\partial_N u^+ = \frac{a^-}{a^+} \partial_N u^- =: \kappa \partial_N u^- \quad (4)$$

where κ will be referred to as ‘‘kink ratio’’ and where we use the notation $\langle \cdot, \cdot \rangle$ for scalar products in \mathbb{R}^d . Moreover, the temperature u is continuous along the interface.

2.2 Locally Admissible Profiles

Let us now consider a point z on the interface between Ω_- and Ω_+ with (unit) normal N and (unit) tangent T , see Figure 1 (middle). Such z will be called *virtual node* to reflect that the node is only used for the construction of basis functions but has no associated degree of freedom (DOF). A locally (in a neighborhood of z) admissible temperature profile has the form

$$u : x \mapsto \begin{cases} \kappa \langle b(x-z), N \rangle + c \langle x-z, T \rangle + d & x \in \Omega_+, \\ \langle b(x-z), N \rangle + c \langle x-z, T \rangle + d & x \in \Omega_-. \end{cases} \quad (5)$$

The space of locally admissible temperature profiles is spanned by the local prototype functions

$$\begin{aligned} \eta_0(x) &= \begin{cases} \kappa \langle x-z, N \rangle & \text{for } x \in \Omega_+ \\ \langle x-z, N \rangle & \text{for } x \in \Omega_- \end{cases} \\ \eta_1(x) &= \langle x-z, T \rangle \\ \eta_2(x) &= 1 \end{aligned} \quad (6)$$

2.3 Simplex-Wise and Local and Interpolation Scheme

Now let $\sigma = (r_0, r_1, r_2)$ be three nodes of a triangle containing an interface point z on an edge. We will apply the following considerations for a triangle generated by the first not interface adapted subdivision of initial regular mesh. Without any restriction, let $r_0, r_2 \in \Omega_-$ and $r_1 \in \Omega_+$, see Figure 1 (middle).

Now, we ask for an interpolation scheme on σ of the form

$$u(z) = w_z^{r_0} u(r_0) + w_z^{r_1} u(r_1) + w_z^{r_2} u(r_2) \quad (7)$$

that is capable of correctly interpolating any locally admissible function. Taking into account the local prototype functions η_i , we obtain the system of linear equations

$$\begin{aligned} \eta_0(z) &= w_z^{r_0} \eta_0(r_0) + w_z^{r_1} \eta_0(r_1) + w_z^{r_2} \eta_0(r_2) \\ \eta_1(z) &= w_z^{r_0} \eta_1(r_0) + w_z^{r_1} \eta_1(r_1) + w_z^{r_2} \eta_1(r_2) \\ \eta_2(z) &= w_z^{r_0} \eta_2(r_0) + w_z^{r_1} \eta_2(r_1) + w_z^{r_2} \eta_2(r_2) \end{aligned} \quad (8)$$

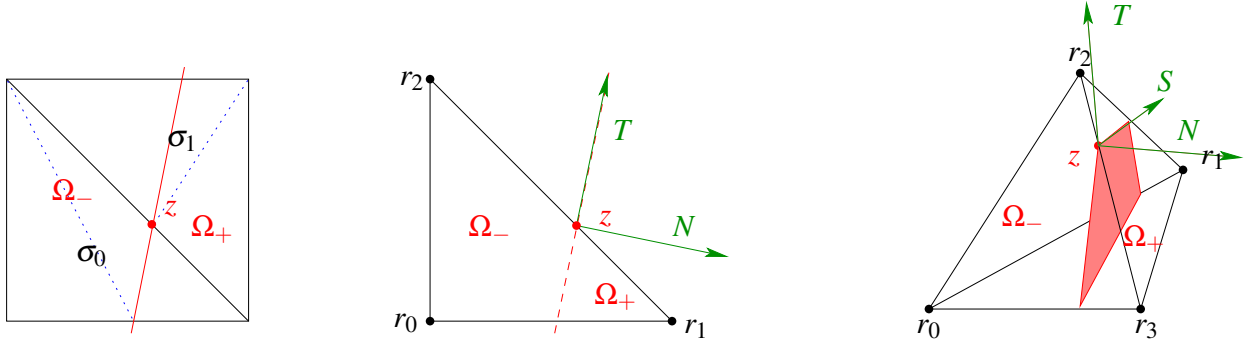


Figure 1: *Left*: Interface (red line) cutting through a square of the regular grid, divided in two regular triangles σ_0, σ_1 subdivided in virtual triangles (by dotted blue line). *Middle*: Normal and tangential directions at a virtual node z in a triangle (r_0, r_1, r_2) . *Right*: One virtual node z lies in a tetrahedron (r_0, \dots, r_3) being cut by an interface (red plane) with normal direction N and tangential directions S and T .

corresponding to the system of equations

$$\begin{bmatrix} \langle r_0 - z, N \rangle & \kappa \langle r_1 - z, N \rangle & \langle r_2 - z, N \rangle \\ \langle r_0 - z, T \rangle & \langle r_1 - z, T \rangle & \langle r_2 - z, T \rangle \\ 1 & 1 & 1 \end{bmatrix} \begin{bmatrix} w_z^{r_0} \\ w_z^{r_1} \\ w_z^{r_2} \end{bmatrix} = \begin{bmatrix} 0 \\ 0 \\ 1 \end{bmatrix} \quad (9)$$

which we can solve for the interpolation weights. Let P_z be the set of adjacent simplices to one virtual node z , cf. Figure 1 (left). In case of a planar interface, the interpolation is exact on any adjacent simplex. If the interface is curved and thus the piecewise planar approximation of the interface is not globally planar, this is no longer true. In either case, arithmetic averaging of the interpolation weights over all adjacent simplices (up to ignoring very thin or small and thus “numerically unreliable simplices”, cf. [24]) can be used to define a local interpolation operator.

Let the notation $w_z^{r,\sigma}$ denote that the interpolation weight from r to z was obtained on the simplex σ . Moreover, let the tilde indicate that the averaged interpolation weights will now be used for a different purpose:

$$\tilde{w}_z^r = \frac{1}{|P_z|} \sum_{\sigma \in P_z} w_z^{r,\sigma} \quad (10)$$

Let $C^{\text{ing}}(z) = \{r \text{ regular node} \mid \tilde{w}_z^r \neq 0\}$ be the set of *constraining regular nodes* (short: *constraints*) of a virtual node z . Interpolation of u from regular nodes r to a virtual node z is then defined as

$$\mathcal{I}[u](z) := \sum_{r \in C^{\text{ing}}(z)} \tilde{w}_z^r u(r). \quad (11)$$

2.4 Composite Finite Element Basis Functions

Starting from the regular hexahedral grid, a *virtual grid* can be defined by first subdividing each cube in six tetrahedra, adding the virtual nodes and introducing additional edges consistently across facets of the cube and in such a way that we obtain a piecewise planar approximation of the interface. This construction is an automatic and purely local operation. Standard piecewise affine basis functions on this virtual grid will be denoted *virtual basis functions* ψ^Δ . The term “virtual” reflects the fact that these will not be used directly for the calculation because the virtual tetrahedra may be of very

low quality (e.g., there is no lower bound on their aspect ratio [30]). DOF are associated only to nodes of the regular hexahedral grid.

Let us now reinterpret the interpolation of Subsection 2.3 to use it for the construction of CFE basis functions: we consider linear combinations of virtual basis functions ψ^Δ (with DOF on the local auxiliary grid) to obtain CFE basis functions ψ^{CFE} (with DOF on the regular rectangular grid only).

For this purpose, let us interpret the interpolation weights in Section 2.3 in a different way: consider a function b with discrete values $b(r) = 1$ at the regular node r and $b(s) = 0$ at all other regular nodes s , then by (11) the interpolation of b at a virtual node z is $\mathcal{I}[b](z) = w_z^r$. Even though such b does not globally satisfy (3), we can use w_z^r as a (coarsening) weight with which the virtual basis function φ_z^Δ contributes to a CFE basis function φ_r^{CFE} .

Let $C(r) = \{z \text{ virtual node} \mid r \in C^{\text{ing}}(z)\} \cup \{r\}$ and $\tilde{w}_r^r := 1$. We define the *Composite Finite Element (CFE) basis functions* as

$$\psi_r^{\text{CFE}}(x) := \sum_{z \in C(r)} \tilde{w}_z^r \psi_z^\Delta(x) \quad (12)$$

and define

$$\mathcal{S}^{\text{CFE}} := \text{span} \{ \psi_r^{\text{CFE}} \mid r \text{ regular node} \}. \quad (13)$$

For two regular nodes r, s , we have $\tilde{w}_s^r = \delta_{rs}$ (with the Kronecker symbol δ). This implies nodality of the basis functions, thus the ψ_r^{CFE} indeed form a basis. Due to the construction, they are piecewise affine with additional kinks at the edges of the virtual grid. The last equation in (9) implies that they form a partition of unity. However, (12) is not a convex combination, thus basis functions may attain negative values; moreover the support of CFE basis functions is still local but larger than for standard piecewise affine FE (resulting in a different sparsity structure of CFE matrices, see Figure 3). Figure 2 shows examples for 2D CFE basis functions.

2.5 Extension to Anisotropic Heat Diffusion

In case of anisotropic heat diffusion (1), the coupling condition is still relative to the orientation of the interface with normal $N = (N_0, N_1)$ and tangent vector $T = (T_0, T_1)$. For the change of the coordinate system from the canonical basis to the basis (N, T) we obtain

$$\begin{aligned} \begin{bmatrix} N_0 & N_1 \\ T_0 & T_1 \end{bmatrix} \begin{bmatrix} \partial_0 u \\ \partial_1 u \end{bmatrix} &= \begin{bmatrix} \partial_N u \\ \partial_T u \end{bmatrix} \\ \Leftrightarrow \begin{bmatrix} \partial_0 u \\ \partial_1 u \end{bmatrix} &= \begin{bmatrix} N_0 & T_0 \\ N_1 & T_1 \end{bmatrix} \begin{bmatrix} \partial_N u \\ \partial_T u \end{bmatrix} =: G \begin{bmatrix} \partial_N u \\ \partial_T u \end{bmatrix} \end{aligned} \quad (14)$$

with the orthonormal 2×2 transformation matrix G . The continuity of the heat flux in normal direction, $\langle \mathcal{A}^+ \nabla u^+, N \rangle = \langle \mathcal{A}^- \nabla u^-, N \rangle$, now reads as follows:

$$\langle \mathcal{A}^+ G \begin{bmatrix} \partial_N u^+ \\ \partial_T u^+ \end{bmatrix}, N \rangle = \langle \mathcal{A}^- G \begin{bmatrix} \partial_N u^- \\ \partial_T u^- \end{bmatrix}, N \rangle. \quad (15)$$

Thus, written in components and using Einstein summation convention we get

$$\mathcal{A}_{ij}^+ N_j N_i \partial_N u^+ + \mathcal{A}_{ij}^+ T_j N_i \partial_T u^+ = \mathcal{A}_{ij}^- N_j N_i \partial_N u^- + \mathcal{A}_{ij}^- T_j N_i \partial_T u^- \quad (16)$$

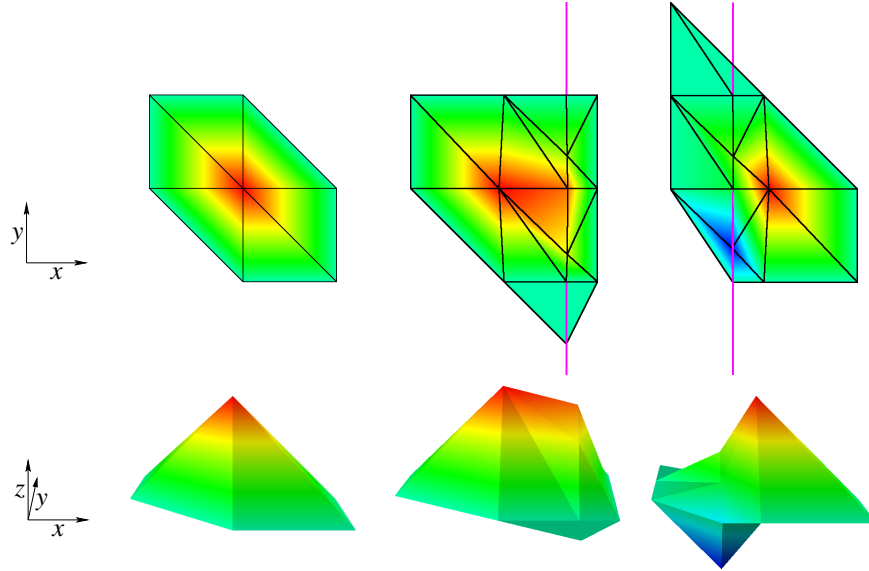


Figure 2: 2D CFE Basis functions are depicted. In the *first row* a top view with the virtual grid is shown, whereas in the *second row* a side view is displayed using a hsv blue-to-red color transition to additionally encode the values of the basis function. Away from the interface, we obtain standard piecewise affine tent functions on the usual cross grid (*left*). Near the interface indicated by magenta lines the CFE construction produces modified basis functions for a kink ratio $\kappa = 10$ (*middle and right*).

so the complete set of of coupling conditions at the point z is given by

$$\begin{aligned} \underbrace{\begin{bmatrix} \mathcal{A}_{ij}^+ N_j N_i & \mathcal{A}_{ij}^+ T_j N_i \\ 0 & 1 \end{bmatrix}}_{=:K^+} \begin{bmatrix} \partial_N u^+ \\ \partial_T u^+ \end{bmatrix} &= \underbrace{\begin{bmatrix} \mathcal{A}_{ij}^- N_j N_i & \mathcal{A}_{ij}^- T_j N_i \\ 0 & 1 \end{bmatrix}}_{=:K^-} \begin{bmatrix} \partial_N u^- \\ \partial_T u^- \end{bmatrix} \\ \Rightarrow \begin{bmatrix} \partial_N u^+ \\ \partial_T u^+ \end{bmatrix} &= (K^+)^{-1} K^- \begin{bmatrix} \partial_N u^- \\ \partial_T u^- \end{bmatrix} =: \begin{bmatrix} K_{NN} & K_{NT} \\ 0 & 1 \end{bmatrix} \begin{bmatrix} \partial_N u^- \\ \partial_T u^- \end{bmatrix} \end{aligned} \quad (17)$$

where K^+ is invertible iff $\mathcal{A}_{ij}^\pm N_j N_i \neq 0$. The entries of K depend on the thermal conductivity tensor A and the local geometry (N, T) .

Again, for the isotropic case $\mathcal{A} = \kappa \mathbb{1}$, Equations (15) and (17) simplify to (3) and (4), respectively. Prototype functions for locally admissible temperature profiles in this case are:

$$\begin{aligned} \eta_0(x) &= \begin{cases} K_{NN} \langle x - z, N \rangle & \text{for } x \in \Omega_+ \\ \langle x - z, N \rangle & \text{for } x \in \Omega_- \end{cases} \\ \eta_1(x) &= \begin{cases} K_{NT} \langle x - z, N \rangle + \langle x - z, T \rangle & \text{for } x \in \Omega_+ \\ \langle x - z, T \rangle & \text{for } x \in \Omega_- \end{cases} \\ \eta_2(x) &= 1 \end{aligned} \quad (18)$$

The remaining construction using these local prototype functions, i.e. setting up and solving a system similar to (9), averaging interpolation weights (10), and defining CFE basis functions (12)) is done in the same manner as before.

2.6 Extension to Heat Diffusion in 3D

In three space dimensions, we have the normal direction N plus two tangential directions S and T , cf. Figure 1 (right). This implies in the isotropic case that locally admissible temperature profiles are of the form

$$u : x \mapsto \begin{cases} \kappa b \langle (x-z), N \rangle + c_0 \langle x-z, S \rangle + c_1 \langle x-z, T \rangle + d & x \in \Omega_+ \\ b \langle (x-z), N \rangle + c_0 \langle x-z, S \rangle + c_1 \langle x-z, T \rangle + d & x \in \Omega_- \end{cases} \quad (19)$$

and can be written as a linear combination of the prototype functions

$$\begin{aligned} \eta_0(x) &= \begin{cases} \kappa \langle x-z, N \rangle & \text{for } x \in \Omega_+ \\ \langle x-z, N \rangle & \text{for } x \in \Omega_- \end{cases}, \\ \eta_1(x) &= \langle x-z, S \rangle, \\ \eta_2(x) &= \langle x-z, T \rangle, \\ \eta_3(x) &= 1. \end{aligned} \quad (20)$$

If we consider a tetrahedron with vertices $r_0, r_2 \in \Omega_-$ and $r_1, r_3 \in \Omega_+$ (see Figure 1, right), we obtain the system of linear equations (cf. Equation (9))

$$\begin{bmatrix} \langle r_0-z, N \rangle & \kappa \langle r_1-z, N \rangle & \langle r_2-z, N \rangle & \kappa \langle r_3-z, N \rangle \\ \langle r_0-z, S \rangle & \langle r_1-z, S \rangle & \langle r_2-z, S \rangle & \langle r_3-z, S \rangle \\ \langle r_0-z, T \rangle & \langle r_1-z, T \rangle & \langle r_2-z, T \rangle & \langle r_3-z, T \rangle \\ 1 & 1 & 1 & 1 \end{bmatrix} \begin{bmatrix} w_z^{r_0} \\ w_z^{r_1} \\ w_z^{r_2} \\ w_z^{r_3} \end{bmatrix} = \begin{bmatrix} 0 \\ 0 \\ 0 \\ 1 \end{bmatrix} \quad (21)$$

to be solved for the interpolation weights $w_z^{r_j}$. Again, the remaining construction is performed as in Subsections 2.3 and 2.4. Now, let us consider the anisotropic case. Using (cf. Equation (14))

$$\begin{bmatrix} \partial_0 u \\ \partial_1 u \\ \partial_2 u \end{bmatrix} = G \begin{bmatrix} \partial_{Nu} \\ \partial_{Su} \\ \partial_{Tu} \end{bmatrix} \quad \text{with} \quad G = \begin{bmatrix} N_0 & S_0 & T_0 \\ N_1 & S_1 & T_1 \\ N_2 & S_2 & T_2 \end{bmatrix}, \quad (22)$$

the anisotropic coupling condition (cf. (17)) is of the form

$$\begin{aligned} & \begin{bmatrix} A_{ij}^+ N_j N_i & A_{ij}^+ S_j N_i & A_{ij}^+ T_j N_i \\ 0 & 1 & 0 \\ 0 & 0 & 1 \end{bmatrix} \begin{bmatrix} \partial_{Nu}^+ \\ \partial_{Su}^+ \\ \partial_{Tu}^+ \end{bmatrix} = \begin{bmatrix} A_{ij}^- N_j N_i & A_{ij}^- S_j N_i & A_{ij}^- T_j N_i \\ 0 & 1 & 0 \\ 0 & 0 & 1 \end{bmatrix} \begin{bmatrix} \partial_{Nu}^- \\ \partial_{Su}^- \\ \partial_{Tu}^- \end{bmatrix} \\ \Rightarrow & \begin{bmatrix} \partial_{Nu}^+ \\ \partial_{Su}^+ \\ \partial_{Tu}^+ \end{bmatrix} =: \begin{bmatrix} K_{NN} & K_{NS} & K_{NT} \\ 0 & 1 & 0 \\ 0 & 0 & 1 \end{bmatrix} \begin{bmatrix} \partial_{Nu}^- \\ \partial_{Su}^- \\ \partial_{Tu}^- \end{bmatrix}. \end{aligned} \quad (23)$$

Locally admissible profiles η are defined in the same manner as in (18) and (20) and the remaining construction is again the same as in the previous subsections.

3 Composite Finite Elements for Linear Elasticity

Linear elasticity is described by the elliptic operator

$$u \mapsto -\operatorname{div}(\mathcal{C}\varepsilon(u)) \quad (24)$$

with the symmetrized gradient (strain) $\varepsilon(u) = \frac{1}{2} [\nabla u + (\nabla u)^T]$ for a displacement u and a fourth-order linear elasticity tensor \mathcal{C} . Coupling conditions are obtained from continuity of u in tangential direction and the equilibrium of forces at the interface, i.e. continuity of the normal stress

$$\mathcal{C}^+ \varepsilon(u^+)N = \mathcal{C}^- \varepsilon(u^-)N \quad (25)$$

across the interface (in normal direction N). We will see that this generally implies a coupling of the derivatives of all spatial components of u . The Lamé-Navier elasticity tensor (isotropic) is given by

$$C_{ijkl} = \lambda \delta_{ij} \delta_{kl} + \mu (\delta_{ik} \delta_{jl} + \delta_{il} \delta_{jk}) \quad \text{with } \lambda = \frac{E \cdot \nu}{(1+\nu)(1-2\nu)}, \mu = \frac{E}{2(1+\nu)} \quad (26)$$

where the Lamé numbers λ, μ depend linearly on Young's modulus E (stiffness) and nonlinearly on Poisson's ratio ν (bulging/volume conservation parameter). Moreover, the normal stress is given by

$$\mathcal{C}\varepsilon(u)N = \lambda(\operatorname{div} u)1N + \mu(\nabla u + \nabla u^T)N = \lambda(\operatorname{div} u)N + \mu(\nabla u + \nabla u^T)N. \quad (27)$$

We are interested in the case where both E and ν are discontinuous across an interface.

3.1 Coupling Condition for Lamé-Navier Elasticity in 2D

Let $N = \begin{bmatrix} N_0 \\ N_1 \end{bmatrix}$ and $T = \begin{bmatrix} T_0 \\ T_1 \end{bmatrix}$, then we can express ∇u in terms of directional derivatives (cf. (14))

$$\nabla u \begin{bmatrix} N_0 & T_0 \\ N_1 & T_1 \end{bmatrix} = \begin{bmatrix} \partial_0 u_0 & \partial_1 u_0 \\ \partial_0 u_1 & \partial_1 u_1 \end{bmatrix} \begin{bmatrix} N_0 & T_0 \\ N_1 & T_1 \end{bmatrix} = \begin{bmatrix} \partial_N u_0 & \partial_T u_0 \\ \partial_N u_1 & \partial_T u_1 \end{bmatrix} \quad (28)$$

so that

$$\begin{aligned} \nabla u &= \begin{bmatrix} \partial_N u_0 & \partial_T u_0 \\ \partial_N u_1 & \partial_T u_1 \end{bmatrix} \begin{bmatrix} N_0 & T_0 \\ N_1 & T_1 \end{bmatrix}^{-1} = \begin{bmatrix} \partial_N u_0 & \partial_T u_0 \\ \partial_N u_1 & \partial_T u_1 \end{bmatrix} \begin{bmatrix} N_0 & N_1 \\ T_0 & T_1 \end{bmatrix} \\ &= \begin{bmatrix} N_0 \partial_N u_0 + T_0 \partial_T u_0 & N_1 \partial_N u_0 + T_1 \partial_T u_0 \\ N_0 \partial_N u_1 + T_0 \partial_T u_1 & N_1 \partial_N u_1 + T_1 \partial_T u_1 \end{bmatrix}, \\ \operatorname{div} u &= \operatorname{tr} \nabla u = N_0 \partial_N u_0 + N_1 \partial_N u_1 + T_0 \partial_T u_0 + T_1 \partial_T u_1. \end{aligned} \quad (29)$$

Hence

$$\begin{aligned} \nabla u + \nabla u^T &= \begin{bmatrix} 2N_0 \partial_N u_0 + 2T_0 \partial_T u_0 & N_1 \partial_N u_0 + T_1 \partial_T u_0 + N_0 \partial_N u_1 + T_0 \partial_T u_1 \\ N_0 \partial_N u_1 + T_0 \partial_T u_1 + N_1 \partial_N u_0 + T_1 \partial_T u_0 & 2N_1 \partial_N u_1 + 2T_1 \partial_T u_1 \end{bmatrix} \\ &= 2\varepsilon(u) =: 2G \begin{bmatrix} \partial_N u_0 & \partial_T u_0 \\ \partial_N u_1 & \partial_T u_1 \end{bmatrix}. \end{aligned} \quad (30)$$

If we let $R = \begin{bmatrix} N_0 & N_1 \\ T_0 & T_1 \end{bmatrix}$, then the fourth-order tensor G is given by $G_{ijkl} = \frac{1}{2} (\delta_{ik} R_{lj} + \delta_{jk} R_{li})$.

Now, we collect the terms necessary for computing $\mathcal{C}\varepsilon(u)N$:

$$(\nabla u + \nabla u^T)N = \begin{bmatrix} (2N_0^2 + N_1^2) \partial_N u_0 + (N_0 N_1) \partial_N u_1 + (2N_0 T_0 + N_1 T_1) \partial_T u_0 + (N_1 T_0) \partial_T u_1 \\ (N_0 N_1) \partial_N u_0 + (N_0^2 + 2N_1^2) \partial_N u_1 + (N_0 T_1) \partial_T u_0 + (N_0 T_0 + 2N_1 T_1) \partial_T u_1 \end{bmatrix},$$

$$(\operatorname{div} u)N = \begin{bmatrix} N_0^2 \partial_N u_0 + N_0 N_1 \partial_N u_1 + N_0 T_0 \partial_T u_0 + N_0 T_1 \partial_T u_1 \\ N_0 N_1 \partial_N u_0 + N_1^2 \partial_N u_1 + N_1 T_0 \partial_T u_0 + N_1 T_1 \partial_T u_1 \end{bmatrix} \quad (31)$$

Making use of the orthonormality of N and T ($N_0^2 + N_1^2 = T_0^2 + T_1^2 = 1$, $N_0 T_0 + N_1 T_1 = 0$) we obtain

$$\mathcal{C}\varepsilon(u)N = \begin{bmatrix} [\lambda N_0^2 + \mu(1 + N_0^2)] \partial_N u_0 + [\lambda N_0 N_1 + \mu N_0 N_1] \partial_N u_1 + \dots \\ \dots + [\lambda N_0 T_0 + \mu N_0 T_0] \partial_T u_0 + [\lambda N_0 T_1 + \mu N_1 T_0] \partial_T u_1 \\ [\lambda N_0 N_1 + \mu N_0 N_1] \partial_N u_0 + [\lambda N_1^2 + \mu(1 + N_1^2)] \partial_N u_1 + \dots \\ \dots + [\lambda N_1 T_0 + \mu N_0 T_1] \partial_T u_0 + [\lambda N_1 T_1 + \mu N_1 T_1] \partial_T u_1 \end{bmatrix}. \quad (32)$$

Hence, the coupling condition across the interface is given by the system of linear equations

$$\begin{bmatrix} \lambda^+ N_0^2 + \mu^+(1 + N_0^2) & \lambda^+ N_0 N_1 + \mu^+ N_0 N_1 & \lambda^+ N_0 T_0 + \mu^+ N_0 T_0 & \lambda^+ N_0 T_1 + \mu^+ N_1 T_0 \\ \lambda^+ N_0 N_1 + \mu^+ N_0 N_1 & \lambda^+ N_1^2 + \mu^+(1 + N_1^2) & \lambda^+ N_1 T_0 + \mu^+ N_0 T_1 & \lambda^+ N_1 T_1 + \mu^+ N_1 T_1 \\ 0 & 0 & 1 & 0 \\ 0 & 0 & 0 & 1 \end{bmatrix} \begin{bmatrix} \partial_N u_0^+ \\ \partial_N u_1^+ \\ \partial_T u_0^+ \\ \partial_T u_1^+ \end{bmatrix} \\ = \begin{bmatrix} \lambda^- N_0^2 + \mu^-(1 + N_0^2) & \lambda^- N_0 N_1 + \mu^- N_0 N_1 & \lambda^- N_0 T_0 + \mu^- N_0 T_0 & \lambda^- N_0 T_1 + \mu^- N_1 T_0 \\ \lambda^- N_0 N_1 + \mu^- N_0 N_1 & \lambda^- N_1^2 + \mu^-(1 + N_1^2) & \lambda^- N_1 T_0 + \mu^- N_0 T_1 & \lambda^- N_1 T_1 + \mu^- N_1 T_1 \\ 0 & 0 & 1 & 0 \\ 0 & 0 & 0 & 1 \end{bmatrix} \begin{bmatrix} \partial_N u_0^- \\ \partial_N u_1^- \\ \partial_T u_0^- \\ \partial_T u_1^- \end{bmatrix}$$

which we abbreviate by $K^+ [\partial_N u_0^+, \partial_N u_1^+, \partial_T u_0^+, \partial_T u_1^+]^T = K^- [\partial_N u_0^-, \partial_N u_1^-, \partial_T u_0^-, \partial_T u_1^-]^T$ and finally obtain

$$\begin{bmatrix} \partial_N u_0^+ \\ \partial_N u_1^+ \\ \partial_T u_0^+ \\ \partial_T u_1^+ \end{bmatrix} = (K^+)^{-1} K^- \begin{bmatrix} \partial_N u_0^- \\ \partial_N u_1^- \\ \partial_T u_0^- \\ \partial_T u_1^- \end{bmatrix} =: \begin{bmatrix} K_{N_0 N_0} & K_{N_0 N_1} & K_{N_0 T_0} & K_{N_0 T_1} \\ K_{N_1 N_0} & K_{N_1 N_1} & K_{N_1 T_0} & K_{N_1 T_1} \\ 0 & 0 & 1 & 0 \\ 0 & 0 & 0 & 1 \end{bmatrix} \begin{bmatrix} \partial_N u_0^- \\ \partial_N u_1^- \\ \partial_T u_0^- \\ \partial_T u_1^- \end{bmatrix} \quad (33)$$

where again the structure of $(K^+)^{-1} K^-$ follows from simple matrix algebra. Clearly, the coupling condition K_{**} depends on N, T (the “direction” of the interface) and λ^\pm, μ^\pm (Lamé-Navier material properties). Let us point out that, in Equation (33), normal and tangential derivatives are even coupled for $\nu^\pm = 0$ (which implies $\lambda^\pm = 0$) and a jump only in E .

Note that K^+ is in fact invertible if the upper left block has strictly positive determinant

$$\begin{aligned} & \det \begin{bmatrix} \lambda^+ N_0^2 + \mu^+(1 + N_0^2) & \lambda^+ N_0 N_1 + \mu^+ N_0 N_1 \\ \lambda^+ N_0 N_1 + \mu^+ N_0 N_1 & \lambda^+ N_1^2 + \mu^+(1 + N_1^2) \end{bmatrix} \\ &= \det \begin{bmatrix} N_0^2(\lambda^+ + \mu^+) + \mu^+ & (\lambda^+ + \mu^+) N_0 N_1 \\ (\lambda^+ + \mu^+) N_0 N_1 & N_1^2(\lambda^+ + \mu^+) + \mu^+ \end{bmatrix} \\ &= (N_0^2(\lambda^+ + \mu^+) + \mu^+) (N_1^2(\lambda^+ + \mu^+) + \mu^+) - ((\lambda^+ + \mu^+) N_0 N_1)^2 \\ &= N_0^2 N_1^2 (\lambda^+ + \mu^+)^2 + \mu^+ (N_0^2 + N_1^2) (\lambda^+ + \mu^+) + (\mu^+)^2 - N_0^2 N_1^2 (\lambda^+ + \mu^+)^2 \\ &= \mu^+ (\lambda^+ + \mu^+) + (\mu^+)^2 > 0 \end{aligned} \quad (34)$$

which is satisfied for physically meaningful values of $E > 0$ and $-1 < \nu < 0.5$.

3.2 Locally Admissible Profiles

Again let us consider a point z on the interface between Ω_- and Ω_+ with (unit) normal N and (unit) tangent T . Locally admissible displacements now lie in the span of

$$\begin{aligned}
 \eta_0(x) &= \begin{cases} \begin{bmatrix} K_{N_0N_0} & 0 \\ K_{N_1N_0} & 0 \\ \langle x-z, N \rangle \\ 0 \end{bmatrix} \begin{bmatrix} \langle x-z, N \rangle \\ \langle x-z, T \rangle \end{bmatrix} \\ \begin{bmatrix} \langle x-z, N \rangle \\ 0 \end{bmatrix} \end{cases}, & \quad \eta_1(x) = \begin{cases} \begin{bmatrix} K_{N_0N_1} & 0 \\ K_{N_1N_1} & 0 \\ 0 \\ \langle x-z, N \rangle \end{bmatrix} \begin{bmatrix} \langle x-z, N \rangle \\ \langle x-z, T \rangle \end{bmatrix} & x \in \Omega_+ \\ \begin{bmatrix} \langle x-z, N \rangle \\ 0 \end{bmatrix} & x \in \Omega_- \end{cases}, \\
 \eta_2(x) &= \begin{cases} \begin{bmatrix} K_{N_0T_0} & 1 \\ K_{N_1T_0} & 0 \\ \langle x-z, T \rangle \\ 0 \end{bmatrix} \begin{bmatrix} \langle x-z, N \rangle \\ \langle x-z, T \rangle \end{bmatrix} \\ \begin{bmatrix} \langle x-z, T \rangle \\ 0 \end{bmatrix} \end{cases}, & \quad \eta_3(x) = \begin{cases} \begin{bmatrix} K_{N_0T_1} & 0 \\ K_{N_1T_1} & 1 \\ 0 \\ \langle x-z, T \rangle \end{bmatrix} \begin{bmatrix} \langle x-z, N \rangle \\ \langle x-z, T \rangle \end{bmatrix} & x \in \Omega_+ \\ \begin{bmatrix} \langle x-z, T \rangle \\ 0 \end{bmatrix} & x \in \Omega_- \end{cases}, \\
 \eta_4(x) &= \begin{bmatrix} 1 \\ 0 \end{bmatrix}, & \quad \eta_5(x) = \begin{bmatrix} 0 \\ 1 \end{bmatrix}.
 \end{aligned} \tag{35}$$

3.3 Simplex-Wise and Local and Interpolation Scheme

Let us again consider the simplex formed by (r_0, r_1, r_2) with $r_0, r_2 \in \Omega_-$ and $r_1 \in \Omega_+$ (cf. Figure 1, right). The simplex-wise interpolation scheme (cf. Equation (7)) is now given by

$$\begin{bmatrix} u_0(z) \\ u_1(z) \end{bmatrix} = W_z^{r_0} \begin{bmatrix} u_0(r_0) \\ u_1(r_0) \end{bmatrix} + W_z^{r_1} \begin{bmatrix} u_0(r_1) \\ u_1(r_1) \end{bmatrix} + W_z^{r_2} \begin{bmatrix} u_0(r_2) \\ u_1(r_2) \end{bmatrix} \tag{36}$$

with interpolation weights $W_z^{r_j}$ which are now 2×2 matrices. We have six prototype functions, each of them with two components. Hence, we obtain twelve equations to determine the twelve unknowns in the interpolation weights: $\eta_i(z) = W_z^{r_0} \eta_i(r_0) + W_z^{r_1} \eta_i(r_1) + W_z^{r_2} \eta_i(r_2) \quad \forall i$ implies

$$\begin{aligned}
 \eta_0 : \quad \begin{bmatrix} 0 \\ 0 \end{bmatrix} &= W_z^{r_0} \begin{bmatrix} \langle r_0-z, N \rangle \\ 0 \end{bmatrix} + W_z^{r_1} \begin{bmatrix} K_{N_0N_0} & 0 \\ K_{N_1N_0} & 0 \end{bmatrix} \begin{bmatrix} \langle r_1-z, N \rangle \\ \langle r_1-z, T \rangle \end{bmatrix} + W_z^{r_2} \begin{bmatrix} \langle r_2-z, N \rangle \\ 0 \end{bmatrix}, \\
 \eta_1 : \quad \begin{bmatrix} 0 \\ 0 \end{bmatrix} &= W_z^{r_0} \begin{bmatrix} 0 \\ \langle r_0-z, N \rangle \end{bmatrix} + W_z^{r_1} \begin{bmatrix} K_{N_0N_1} & 0 \\ K_{N_1N_1} & 0 \end{bmatrix} \begin{bmatrix} \langle r_1-z, N \rangle \\ \langle r_1-z, T \rangle \end{bmatrix} + W_z^{r_2} \begin{bmatrix} 0 \\ \langle r_2-z, N \rangle \end{bmatrix}, \\
 \eta_2 : \quad \begin{bmatrix} 0 \\ 0 \end{bmatrix} &= W_z^{r_0} \begin{bmatrix} \langle r_0-z, T \rangle \\ 0 \end{bmatrix} + W_z^{r_1} \begin{bmatrix} K_{N_0T_0} & 1 \\ K_{N_1T_0} & 0 \end{bmatrix} \begin{bmatrix} \langle r_1-z, N \rangle \\ \langle r_1-z, T \rangle \end{bmatrix} + W_z^{r_2} \begin{bmatrix} \langle r_2-z, T \rangle \\ 0 \end{bmatrix}, \\
 \eta_3 : \quad \begin{bmatrix} 0 \\ 0 \end{bmatrix} &= W_z^{r_0} \begin{bmatrix} 0 \\ \langle r_0-z, T \rangle \end{bmatrix} + W_z^{r_1} \begin{bmatrix} K_{N_0T_1} & 0 \\ K_{N_1T_1} & 1 \end{bmatrix} \begin{bmatrix} \langle r_1-z, N \rangle \\ \langle r_1-z, T \rangle \end{bmatrix} + W_z^{r_2} \begin{bmatrix} 0 \\ \langle r_2-z, T \rangle \end{bmatrix}, \\
 \eta_4 : \quad \begin{bmatrix} 1 \\ 0 \end{bmatrix} &= W_z^{r_0} \begin{bmatrix} 1 \\ 0 \end{bmatrix} + W_z^{r_1} \begin{bmatrix} 1 \\ 0 \end{bmatrix} + W_z^{r_2} \begin{bmatrix} 1 \\ 0 \end{bmatrix}, \\
 \eta_5 : \quad \begin{bmatrix} 0 \\ 1 \end{bmatrix} &= W_z^{r_0} \begin{bmatrix} 0 \\ 1 \end{bmatrix} + W_z^{r_1} \begin{bmatrix} 0 \\ 1 \end{bmatrix} + W_z^{r_2} \begin{bmatrix} 0 \\ 1 \end{bmatrix}.
 \end{aligned} \tag{37}$$

The resulting weights are general 2×2 matrices, in particular they are not symmetric or even diagonal.

3.4 CFE Basis Functions for Linear Elasticity

To build continuous CFE basis functions, we apply the same averaging scheme as in Equation (10), now applied to the matrix valued weights and obtain

$$\tilde{W}_z^r = \frac{1}{|P_z|} \sum_{\sigma \in P_z} W_z^{r,\sigma}. \quad (38)$$

Finally, the CFE interpolation operator (cf. Equation (11)) is defined as follows

$$\mathcal{I} \begin{bmatrix} u_0 \\ u_1 \end{bmatrix} (z) := \sum_{r \in C^{\text{ing}}(z)} \tilde{W}_z^r \begin{bmatrix} u_0(r) \\ u_1(r) \end{bmatrix}. \quad (39)$$

Let $\Psi_{z;\alpha}^\Delta := \psi_z^\Delta \vec{e}_\alpha$ be a standard tent function on the virtual grid “in space direction α ” and $\tilde{W}_r^r = 1$ for regular nodes r . Then the vector-valued CFE basis functions (cf. (12)) are constructed via

$$\Psi_{r;\alpha}^{\text{CFE}}(x) = \sum_{z \in C(r)} \tilde{W}_z^r \Psi_{z;\alpha}^\Delta(x) = \sum_{z \in C(r)} \psi_z^\Delta(x) \tilde{W}_z^r \vec{e}_\alpha. \quad (40)$$

Note that a single virtual basis function $\Psi_{z;\alpha}^\Delta$ only discretizes displacement in one space direction α whereas a single CFE basis function $\Psi_{r;\alpha}^{\text{CFE}}$ (near the interface) may have contributions in all three space directions because the weights \tilde{W}_z^r are not diagonal.

Again, $\tilde{W}_s^r = \delta_{rs} \mathbb{1}$ implies nodality of the basis functions (which thus in fact form a basis), the bottom four equations in (37) imply that they form a partition of unity.

3.5 Extension to Anisotropic Linear Elasticity

In an anisotropic linear elasticity setting, the normal stress condition (25) still holds. Using G defined in Equation (30), we obtain (cf. (27))

$$\mathcal{C}^+ G \begin{bmatrix} \partial_N u_0^+ & \partial_T u_0^+ \\ \partial_N u_1^+ & \partial_T u_1^+ \end{bmatrix} N = \mathcal{C}^- G \begin{bmatrix} \partial_N u_0^- & \partial_T u_0^- \\ \partial_N u_1^- & \partial_T u_1^- \end{bmatrix} N \quad (41)$$

or, in components:

$$\mathcal{C}_{ijkl}^+ G_{klmn} \begin{bmatrix} \partial_N u_0^+ & \partial_T u_0^+ \\ \partial_N u_1^+ & \partial_T u_1^+ \end{bmatrix}_{mn} N_j = \mathcal{C}_{ijkl}^- G_{klmn} \begin{bmatrix} \partial_N u_0^- & \partial_T u_0^- \\ \partial_N u_1^- & \partial_T u_1^- \end{bmatrix}_{mn} N_j. \quad (42)$$

Expanding both sides of (42) (a vector of length 2) yields more complicated expressions than (32), but it is obviously still linear in $\partial_{\{N,T\}} u_{\{0,1\}}$. Hence it can be rewritten in the same way as above in (33). The remaining construction is done in the same fashion as in the previous Subsections 3.2, 3.3, and 3.4.

3.6 Extension to 3D Anisotropic Elasticity

In 3D, let again N be the normal and S, T be two tangential directions so that N, S, T are orthonormal. Using (29) we can define the fourth-order tensor G as the 3D analog of (30):

$$2\mathcal{E}(u) = \nabla u + \nabla u^T =: G \begin{bmatrix} \partial_N u_0 & \partial_S u_0 & \partial_T u_0 \\ \partial_N u_1 & \partial_S u_1 & \partial_T u_1 \\ \partial_N u_2 & \partial_S u_2 & \partial_T u_2 \end{bmatrix}. \quad (43)$$

Let us now only consider general anisotropic linear elasticity. The normal stress can then be written in the form (cf. Equation (32))

$$\begin{aligned} \mathcal{C}\varepsilon(u)N &= \mathcal{C}_{ijkl}G_{klmn} \begin{bmatrix} \partial_N u_0 & \partial_S u_0 & \partial_T u_0 \\ \partial_N u_1 & \partial_S u_1 & \partial_T u_1 \\ \partial_N u_2 & \partial_S u_2 & \partial_T u_2 \end{bmatrix}_{mn} N_j \\ &= \begin{bmatrix} m_{\mathcal{C},N,S,T}^{(0)}(\partial_N u_0, \partial_N u_1, \partial_N u_2, \partial_S u_0, \partial_S u_1, \partial_S u_2, \partial_T u_0, \partial_T u_1, \partial_T u_2) \\ m_{\mathcal{C},N,S,T}^{(1)}(\partial_N u_0, \partial_N u_1, \partial_N u_2, \partial_S u_0, \partial_S u_1, \partial_S u_2, \partial_T u_0, \partial_T u_1, \partial_T u_2) \\ m_{\mathcal{C},N,S,T}^{(2)}(\partial_N u_0, \partial_N u_1, \partial_N u_2, \partial_S u_0, \partial_S u_1, \partial_S u_2, \partial_T u_0, \partial_T u_1, \partial_T u_2) \end{bmatrix} \end{aligned} \quad (44)$$

where the $m_{\mathcal{C},N,S,T}^{(j)}$ are linear in each partial derivative of each component of u with coefficients depending on $\mathcal{C}^\pm, N, S,$ and T . The continuity of normal stress can be expressed as (cf. (42))

$$\mathcal{C}_{ijkl}^+ G_{klmn} \begin{bmatrix} \partial_N u_0^+ & \partial_S u_0^+ & \partial_T u_0^+ \\ \partial_N u_1^+ & \partial_S u_1^+ & \partial_T u_1^+ \\ \partial_N u_2^+ & \partial_S u_2^+ & \partial_T u_2^+ \end{bmatrix}_{mn} N_j = \mathcal{C}_{ijkl}^- G_{klmn} \begin{bmatrix} \partial_N u_0^- & \partial_S u_0^- & \partial_T u_0^- \\ \partial_N u_1^- & \partial_S u_1^- & \partial_T u_1^- \\ \partial_N u_2^- & \partial_S u_2^- & \partial_T u_2^- \end{bmatrix}_{mn} N_j \quad (45)$$

and we obtain a coupling condition of three equations for the normal direction, plus six equations from the continuity in tangential direction. Both in case of Lamé-Navier elasticity and for the fully anisotropic linear case, the normal stress is of the same form as in Equation (33):

$$\begin{bmatrix} \partial_N u_0^+ \\ \partial_N u_1^+ \\ \partial_N u_2^+ \\ \partial_S u_0^+ \\ \partial_S u_1^+ \\ \partial_S u_2^+ \\ \partial_T u_0^+ \\ \partial_T u_1^+ \\ \partial_T u_2^+ \end{bmatrix} = \begin{bmatrix} K_{N_0 N_0} & K_{N_0 N_1} & K_{N_0 N_2} & K_{N_0 S_0} & K_{N_0 S_1} & K_{N_0 S_2} & K_{N_0 T_0} & K_{N_0 T_1} & K_{N_0 T_2} \\ K_{N_1 N_0} & K_{N_1 N_1} & K_{N_1 N_2} & K_{N_1 S_0} & K_{N_1 S_1} & K_{N_1 S_2} & K_{N_1 T_0} & K_{N_1 T_1} & K_{N_1 T_2} \\ K_{N_2 N_0} & K_{N_2 N_1} & K_{N_2 N_2} & K_{N_2 S_0} & K_{N_2 S_1} & K_{N_2 S_2} & K_{N_2 T_0} & K_{N_2 T_1} & K_{N_2 T_2} \\ 0 & 0 & 0 & 1 & 0 & 0 & 0 & 0 & 0 \\ 0 & 0 & 0 & 0 & 1 & 0 & 0 & 0 & 0 \\ 0 & 0 & 0 & 0 & 0 & 1 & 0 & 0 & 0 \\ 0 & 0 & 0 & 0 & 0 & 0 & 1 & 0 & 0 \\ 0 & 0 & 0 & 0 & 0 & 0 & 0 & 1 & 0 \\ 0 & 0 & 0 & 0 & 0 & 0 & 0 & 0 & 1 \end{bmatrix} \begin{bmatrix} \partial_N u_0^- \\ \partial_N u_1^- \\ \partial_N u_2^- \\ \partial_S u_0^- \\ \partial_S u_1^- \\ \partial_S u_2^- \\ \partial_T u_0^- \\ \partial_T u_1^- \\ \partial_T u_2^- \end{bmatrix} \quad (46)$$

Locally admissible displacements now lie in the span of the following local prototype functions η_0, \dots, η_{11} with ($j = 0, 1, 2$) (cf. (35)):

$$\begin{aligned} \eta_{0+j}(x) &= \begin{cases} \begin{bmatrix} K_{N_0 N_j} & 0 & 0 \\ K_{N_1 N_j} & 0 & 0 \\ K_{N_2 N_j} & 0 & 0 \end{bmatrix} \begin{bmatrix} \langle x-z, N \rangle \\ \langle x-z, S \rangle \\ \langle x-z, T \rangle \end{bmatrix} & x \in \Omega_+ \\ \langle x-z, N \rangle \vec{e}_j & x \in \Omega_- \end{cases}, \\ \eta_{3+j}(x) &= \begin{cases} \begin{bmatrix} K_{N_0 S_j} & \delta_{0j} & 0 \\ K_{N_1 S_j} & \delta_{1j} & 0 \\ K_{N_2 S_j} & \delta_{2j} & 0 \end{bmatrix} \begin{bmatrix} \langle x-z, N \rangle \\ \langle x-z, S \rangle \\ \langle x-z, T \rangle \end{bmatrix} & x \in \Omega_+ \\ \langle x-z, S \rangle \vec{e}_j & x \in \Omega_- \end{cases}, \\ \eta_{6+j}(x) &= \begin{cases} \begin{bmatrix} K_{N_0 T_j} & 0 & \delta_{0j} \\ K_{N_1 T_j} & 0 & \delta_{1j} \\ K_{N_2 T_j} & 0 & \delta_{2j} \end{bmatrix} \begin{bmatrix} \langle x-z, N \rangle \\ \langle x-z, S \rangle \\ \langle x-z, T \rangle \end{bmatrix} & x \in \Omega_+ \\ \langle x-z, T \rangle \vec{e}_j & x \in \Omega_- \end{cases}, \\ \eta_{9+j}(x) &= \vec{e}_j. \end{aligned} \quad (47)$$

In the same manner as before, we now need to determine an interpolation scheme

$$\begin{bmatrix} u_0(z) \\ u_1(z) \\ u_2(z) \end{bmatrix} = W_z^{r_0} \begin{bmatrix} u_0(r_0) \\ u_1(r_0) \\ u_2(r_0) \end{bmatrix} + W_z^{r_1} \begin{bmatrix} u_0(r_1) \\ u_1(r_1) \\ u_2(r_1) \end{bmatrix} + W_z^{r_2} \begin{bmatrix} u_0(r_2) \\ u_1(r_2) \\ u_2(r_2) \end{bmatrix} + W_z^{r_3} \begin{bmatrix} u_0(r_3) \\ u_1(r_3) \\ u_2(r_3) \end{bmatrix} \quad (48)$$

where the 36 unknown entries of the four interpolation weights in the $W_z^{r_j}$ are determined by plugging the spanning functions η into (48) which yields $12 \cdot 3 = 36$ equations. Again, we go through the same remaining construction as in Subsections 3.2, 3.3, and 3.4.

4 Assembling CFE Matrices

In the implementation, neither the virtual grid nor the CFE basis functions are explicitly stored. The CFE basis functions are temporarily and locally constructed to assemble the finite element matrices. Here we consider the assembly of the corresponding mass and stiffness matrices, which enables the solution of linear elliptic but also linear parabolic problems with implicit time discretization. We confine here to the most general case of linear elasticity and do not detail the case of scalar problems. Entries of the FE mass matrix M and stiffness matrix L for the heat conduction case are defined as follows:

$$M_{rs} = \int_{\Omega} \psi_r^{\text{CFE}} \psi_s^{\text{CFE}} = \sum_{z \in C(r)} \sum_{y \in C(s)} w_z^r w_y^s \int_{\Omega} \psi_z^{\Delta} \psi_y^{\Delta}, \quad (49)$$

$$L_{rs} = \int_{\Omega} a(x) \nabla \psi_r^{\text{CFE}} \cdot \nabla \psi_s^{\text{CFE}} = \sum_{z \in C(r)} \sum_{y \in C(s)} w_z^r w_y^s \int_{\Omega} a(x) \sum_i \partial_i \psi_z^{\Delta} \partial_i \psi_y^{\Delta}. \quad (50)$$

The global matrices are assembled using the usual element-by-element technique of computing per-element contributions and summing them up in the global matrix. We can make use of the fact that rows corresponding to nodes sufficiently far from the interface are essentially identical throughout Ω_- and Ω_+ (and need to be stored only once), for this and further algorithmic aspects we refer to [17].

Mass Matrices. Recalling Equation (40), we can write the (block) mass matrix for the elasticity problem as follows

$$\begin{aligned} (M_{\alpha\beta})_{rs} &= \int_{\Omega} \Psi_{r;\alpha}^{\text{CFE}} \Psi_{s;\beta}^{\text{CFE}} = \int_{\Omega} \left(\sum_{z \in C(r)} \tilde{W}_z^r \psi_z^{\Delta} \vec{e}_{\alpha} \right) \cdot \left(\sum_{y \in C(s)} \tilde{W}_y^s \psi_y^{\Delta} \vec{e}_{\beta} \right) \\ &= \sum_{z \in C(r)} \sum_{y \in C(s)} \underbrace{\sum_k (\tilde{W}_z^r)_{k\alpha} (\tilde{W}_y^s)_{k\beta}}_{=(\tilde{W}_z^r)^T \tilde{W}_y^s}_{\alpha\beta} \int_{\Omega} \psi_z^{\Delta} \psi_y^{\Delta}. \end{aligned} \quad (51)$$

Note that $M_{\alpha\beta}$ has 3×3 block structure with nonzero off-diagonal blocks.

Elasticity Matrices. For the linear elasticity matrix, we have to evaluate

$$\begin{aligned} (L_{\alpha\beta})_{rs} &= \int_{\Omega} \mathcal{C} \varepsilon(\Psi_{r;\alpha}^{\text{CFE}}) : \varepsilon(\Psi_{s;\beta}^{\text{CFE}}) \\ &= \int_{\Omega} \sum_{klmn} \frac{\mathcal{C}_{klmn}}{4} \left[\partial_m (\Psi_{r;\alpha}^{\text{CFE}})_n + \partial_n (\Psi_{r;\alpha}^{\text{CFE}})_m \right] \left[\partial_k (\Psi_{s;\beta}^{\text{CFE}})_l + \partial_l (\Psi_{s;\beta}^{\text{CFE}})_k \right] \end{aligned} \quad (52)$$

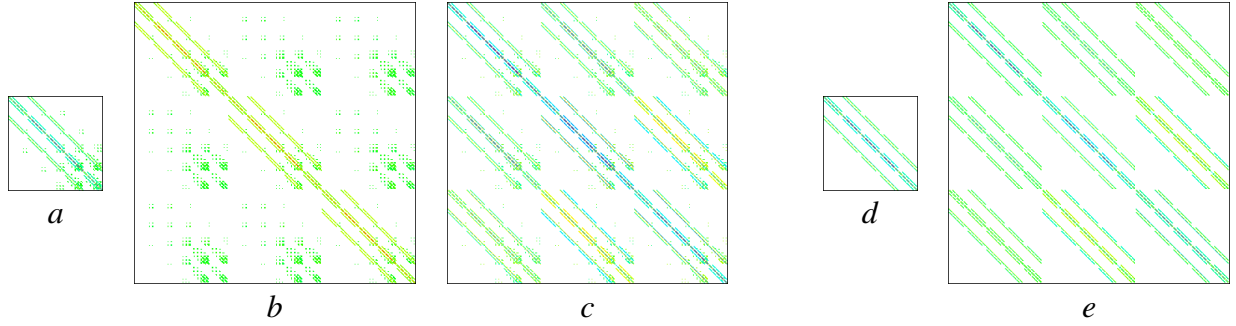


Figure 3: Visualization of (a) a CFE stiffness matrix for jumping heat conduction coefficient with $\kappa = 2$, (b) a CFE mass matrix and (c) a CFE elasticity stiffness matrix for $(E^-, \nu^-) = (1.0, 0.3)$ and $(E^-, \nu^-) = (1.5, 0.1)$ are shown. For comparison, (d) an affine FE stiffness matrix and (e) a CFE elasticity stiffness matrix for a complicated domain and $(E, \nu) = (1.0, 0.3)$ are also shown. A nonlinear HSV blue-to-red color scale  represents the values of nonzero entries where green are entries almost equal to zero and white are entries exactly equal to zero.

and hence terms of the form

$$\begin{aligned} \int_{\Omega} \left[\partial_m (\Psi_{r;\alpha}^{\text{CFE}})_n \right] \left[\partial_k (\Psi_{s;\beta}^{\text{CFE}})_l \right] &= \int_{\Omega} \left[\sum_{z \in C(r)} (\tilde{W}_z^r)_{n\alpha} \partial_m \psi_z^{\Delta} \right] \left[\sum_{y \in C(s)} (\tilde{W}_y^s)_{l\beta} \partial_k \psi_y^{\Delta} \right] \\ &= \sum_{z \in C(r)} \sum_{y \in C(s)} (\tilde{W}_z^r)_{n\alpha} (\tilde{W}_y^s)_{l\beta} \int_{\Omega} \partial_m \psi_z^{\Delta} \partial_k \psi_y^{\Delta} \end{aligned} \quad (53)$$

have to be computed. Finally, we obtain

$$(L_{\alpha\beta})_{rs} = \sum_{zy} \sum_{klmn} \frac{C_{klmn}}{4} \left[\begin{aligned} &(\tilde{W}_z^r)_{n\alpha} (\tilde{W}_y^s)_{l\beta} \int_{\Omega} \partial_m \psi_z^{\Delta} \partial_k \psi_y^{\Delta} + (\tilde{W}_z^r)_{n\alpha} (\tilde{W}_y^s)_{k\beta} \int_{\Omega} \partial_m \psi_z^{\Delta} \partial_l \psi_y^{\Delta} \\ &+ (\tilde{W}_z^r)_{m\alpha} (\tilde{W}_y^s)_{l\beta} \int_{\Omega} \partial_n \psi_z^{\Delta} \partial_k \psi_y^{\Delta} + (\tilde{W}_z^r)_{m\alpha} (\tilde{W}_y^s)_{k\beta} \int_{\Omega} \partial_n \psi_z^{\Delta} \partial_l \psi_y^{\Delta} \end{aligned} \right]. \quad (54)$$

In Figure 3 we visualize the sparsity structure of CFE matrices compared to affine FE and CFE for complicated domains [17] with 15-band structures in each block. The underlying grid is a discretization of $[0, 1]^3$ using 5^3 nodes and interface at $|x| = 0.8\sqrt{3}$. CFE for interior interfaces yield a significantly denser band structure compared to CFE on complicated domains. Moreover, off-diagonal blocks in the block mass matrix (c) contain nonzero entries corresponding to nodes near the interface.

5 Numerical Results

One major advantage of the structured hexahedral grid underlying the CFE computation is the underlying hierarchy of meshes. This in particular permits the use of geometric multigrid strategies [4, 38, 39, 11] for solving or preconditioning. For the scalar heat conduction problems, we have so far used standard coarsening (applying the same weights as for piecewise affine finite elements, which are not adapted to the interface) up to some fixed coarse resolution and used one $(3, V, 3)$ cycle with Block-Gauß-Seidel smoothing in a preconditioned conjugate gradient solver to improve convergence. For the vector-valued case, we have so far used a preconditioned conjugate gradient solver with block-SSOR preconditioning [13]. A four-stripe zebra-type ordering of the unknowns [7] can be used for parallelizing the preconditioner. The results were visualized using POV-Ray and VTK.

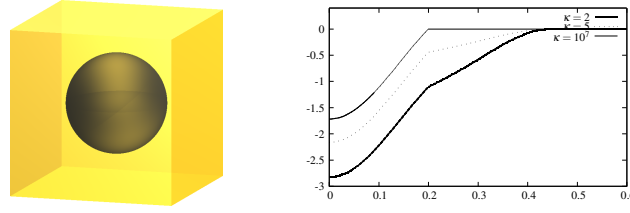


Figure 4: Interface and spherical profile of function to be approximated.

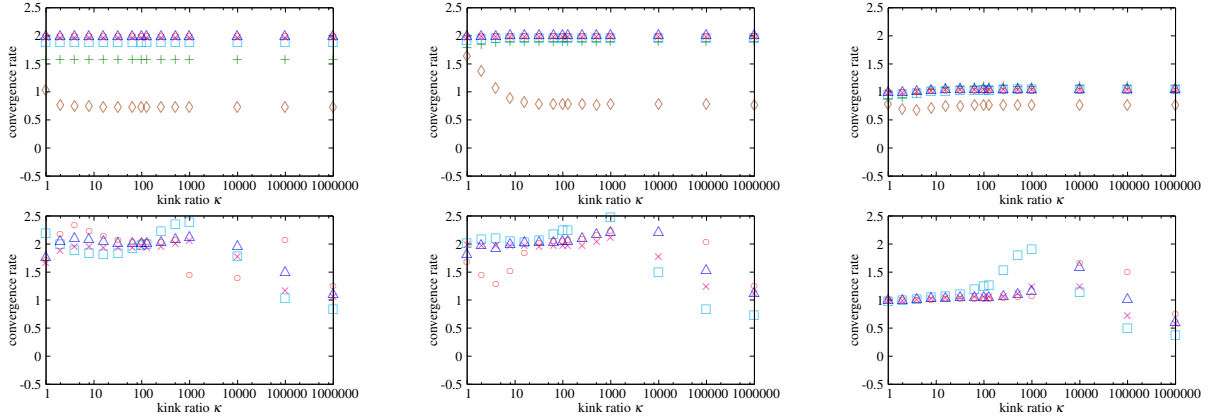


Figure 5: Approximation quality: Estimated convergence orders for the difference between CFE approximation and a given analytic function (*middle row*) and the CFE solution of an elliptic boundary value problem and the analytic solution (*bottom row*) for kink ratios ranging between 1 (no kink) and 10^6 measured in L^∞ , L^2 , and H^1 norm when refining the grid: 5^3 \diamond 9^3 $+$ 17^3 \square 33^3 \times 65^3 \triangle 129^3 \circ 257^3 .

Approximation of a Given Function. Let us consider the spherically-symmetric function with a kink across the spherical interface shown (cf. Figure 4). If we compute the error between the analytic function and its CFE approximation at different resolutions, we observe second order convergence in the L^∞ and L^2 norm and first order convergence in the H^1 norm, where the approximation order breaks down in case of standard affine or multilinear FE on the same regular hexahedral grid. Due to the built-in averaging at non-planar interfaces, the approximation quality depends on the range of kink ratios. In explicit, we do not expect a proper approximation for very large kink ratios.

Heat Conduction Simulation

As an example for a heat conduction simulation, let us consider a hexahedral sample of aluminum foam (Al) embedded in polymethylmethacrylate (PMMA) with edge length 6.81 mm, resolved by 257^3 voxels. A time-dependent heat conduction problem is then described by the partial differential equation initial and boundary value problem

$$\begin{aligned}
 \partial_t [\rho c(x)u(x,t)] &= \operatorname{div} [\lambda(x)\nabla u] && \text{in } \Omega, \\
 u(x,0) &= 293.15 && \text{in } \Omega, \\
 u(\text{bottom},t) &= 194.65 && t > 0, \\
 u(\text{top},t) &= 373.15 && t > 0, \\
 \partial_{\nu(x)}u(x,t) &= 0 && \text{elsewhere on } \partial\Omega
 \end{aligned} \tag{55}$$

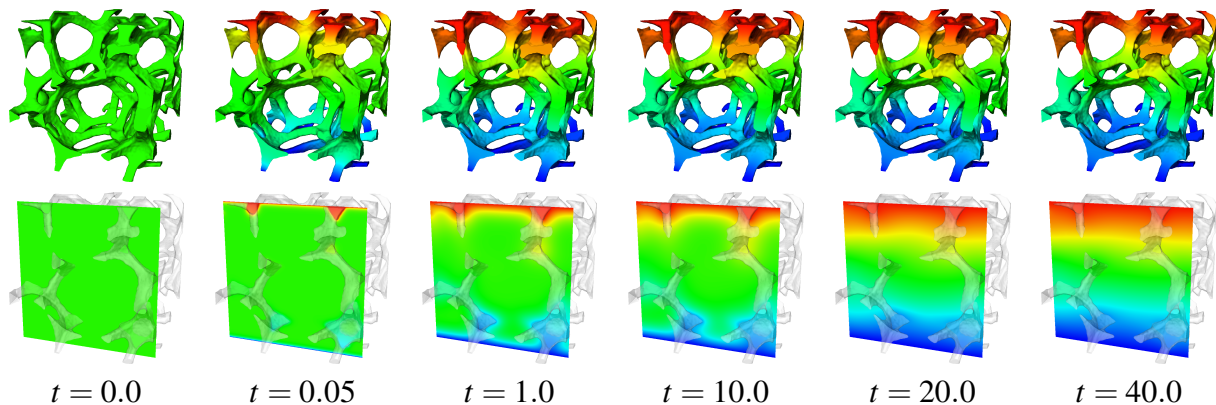


Figure 6: Results of a time-dependent heat conduction simulation on an aluminum foam embedded in PMMA. An almost steady state is reached much faster in the aluminum than in the PMMA.

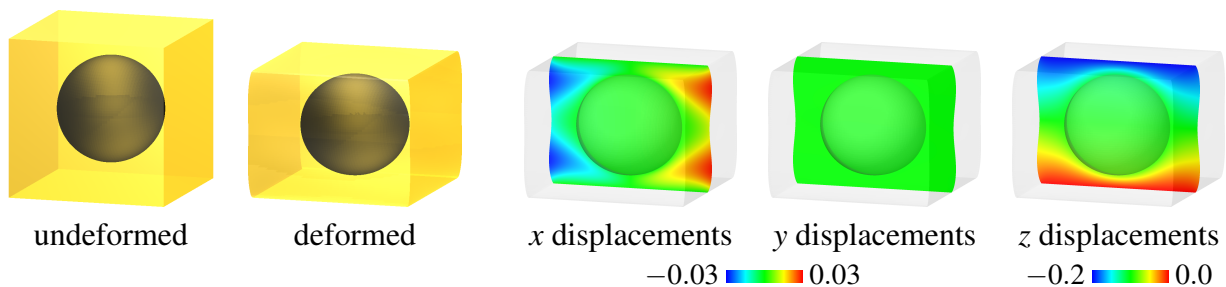


Figure 7: Results of an elasticity simulation: Compression of a sphere ($E_o = 10.0, \nu_o = 0.1$) embedded in a cube ($E_{\square} = 1.0, \nu_{\square} = 0.3$) by 20 %.

with volume-specific heat capacity $\rho c = \{2.43, 1.75\} \cdot 10^6$ J/m³ K for aluminum and PMMA, respectively, and thermal conductivities $\lambda = \{237.0, 0.19\}$ W/m K (thus a kink of ratio 1247 in λ). A visualization of the geometry and the temperature distribution at different times is shown in Figure 6. The figure shows the development of the temperature distribution towards a steady state with fast heat flux through the Al and slower heat flux through the PMMA.

Elasticity Simulation

As a first (toy) example, let us consider a spherical object (radius 0.3 m) with $E_o = 10$ Pa and $\nu_o = 0.1$ embedded in a cube of edge length 1 m with ($E_{\square} = 1$ Pa and $\nu_{\square} = 0.3$), where the bottom face is fixed and the top face is loaded with a downward displacement of 0.2 m. Figure 7 shows the undeformed and deformed objects and a visualization of the displacements. Computational resolution for this example was 65^3 , resulting in a memory requirement of 572 MB.

Let us also consider an Al foam embedded in PMMA for an elasticity simulation. We consider a specimen of $6 \times 6 \times 9.6$ mm at resolution 100 μ m, i.e. computational resolution $60 \times 60 \times 96$. Both materials are assumed to be isotropic with $E_{Al} = 70$ GPa and $\nu_{Al} = 0.35$, $E_{PMMA} = 3$ GPa and $\nu_{PMMA} = 0.38$, subject to 1 % compression in longitudinal direction, cf. Figure 8.

Furthermore, let us consider an elasticity tensor which is discontinuous across an interface and also varies continuously within one material. To show the difference to constant elasticity tensor in each material, we first run a compression (20 %) simulation on a circular column as shown in Figure 10. In the upper row we assume isotropic elasticity with $E_{\square} = 1$ Pa and $\nu_{\square} = 0.38$ in the surrounding material and $E_o = 10$ Pa and $\nu_o = 0.33$ at the top and bottom of the column, linearly

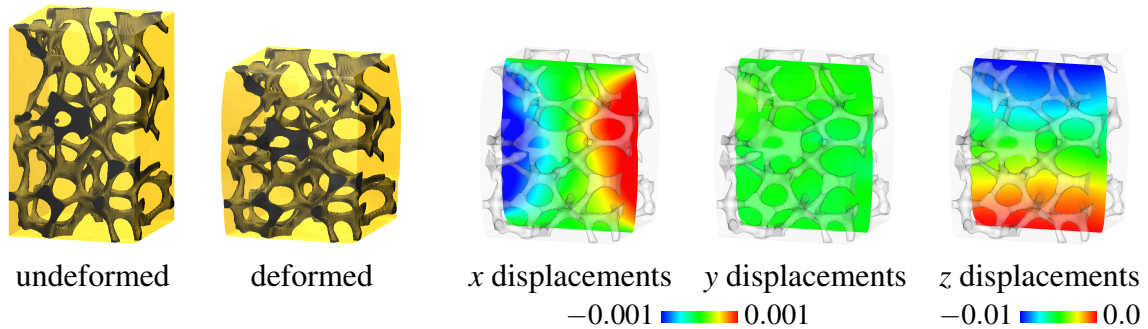


Figure 8: Results of an elasticity simulation on an Al foam ($E_{\text{Al}} = 70$ GPa, $\nu_{\text{Al}} = 0.35$) embedded in PMMA ($E_{\text{PMMA}} = 3$ GPa, $\nu_{\text{PMMA}} = 0.38$) subject to 1 % compression, here shown scaled by a factor 20.

varying to the transversely isotropic tensor V_C listed in Figure 9 in the center (corresponding to half the compressive stiffness in transverse direction). In contrast, in the lower row, the elasticity tensor for the column is constant to the value at top and bottom above. Combined with the surrounding material, this leads to slightly less bulging of the column for the constant-isotropic column.

Finally, let us consider the $5 \times 5 \times 5$ grid of circular rods shown in Figure 11 subject to rotation by 20 degrees (which is intended to enhance the visualization; in reality, this is outside the range where a linear model is valid). For the trabecular centers, we assume transversely isotropic elasticity tensors V_T (cf. Figure 9) of vertebral trabecular bone [36], rotated accordingly; averaged to an isotropic tensor in the trabecular crossings and interpolated trilinearly. The embedding material is assumed to be isotropic PMMA with $E_{\text{PMMA}} = 3$ GPa and $\nu_{\text{PMMA}} = 0.38$.

6 Conclusions

This paper shows the construction of Composite FE basis functions for simulating different physical processes on objects with geometrically complicated interfaces between different materials. CFE show optimal convergence behavior for the interpolation error for piecewise affine interpolation. We consider applications to artificially constructed objects described by level set functions [21] and real objects described by μCT scans. In both cases, the construction of CFE basis functions is fully automatic and the simulations profit from efficient data structures for the underlying regular hexahedral computational grid.

The construction presented here is limited to linear problems and piecewise affine (C)FE basis functions. We have only discussed the case of a single material interface, the extension to multiple (separated) interfaces, however, is straightforward. Our current implementation can only deal with cuboid domains with a complicated interface inside, but it is possible to combine CFE for discontinuous coefficients and CFE for complicated domains [17, 25], see [22], to treat more general shapes. Boundary conditions are applied to the outside of the (cuboid) specimen, but besides the coupling, no additional boundary conditions are prescribed to the interface.

Further research will include the application of CFE to homogenization, i.e. determining effective material properties of specimens with microstructure, as previously studied in [27]. There is still potential to improve the preconditioning and solver strategies and optimize the C++ implementation and parallelization. Moreover, validation of the method still has to be performed.

$$V_C := \begin{pmatrix} 7.408 & 3.649 & 3.649 & & & \\ 3.649 & 7.408 & 3.649 & & & \\ 7.298 & 7.298 & 14.82 & & & \\ & & & 3.759 & & \\ & & & & 3.759 & \\ & & & & & 1.880 \end{pmatrix} \quad V_T := \begin{pmatrix} 19.78 & 8.419 & 8.419 & & & \\ 8.419 & 16.18 & 7.615 & & & \\ 8.419 & 7.615 & 16.18 & & & \\ & & & 8.567 & & \\ & & & & 9.471 & \\ & & & & & 9.471 \end{pmatrix}$$

Figure 9: Transversely isotropic elasticity tensors in GPa in Voigt’s notation [34] used for the simulations in Figures 10 (V_C) and 11 (V_T).

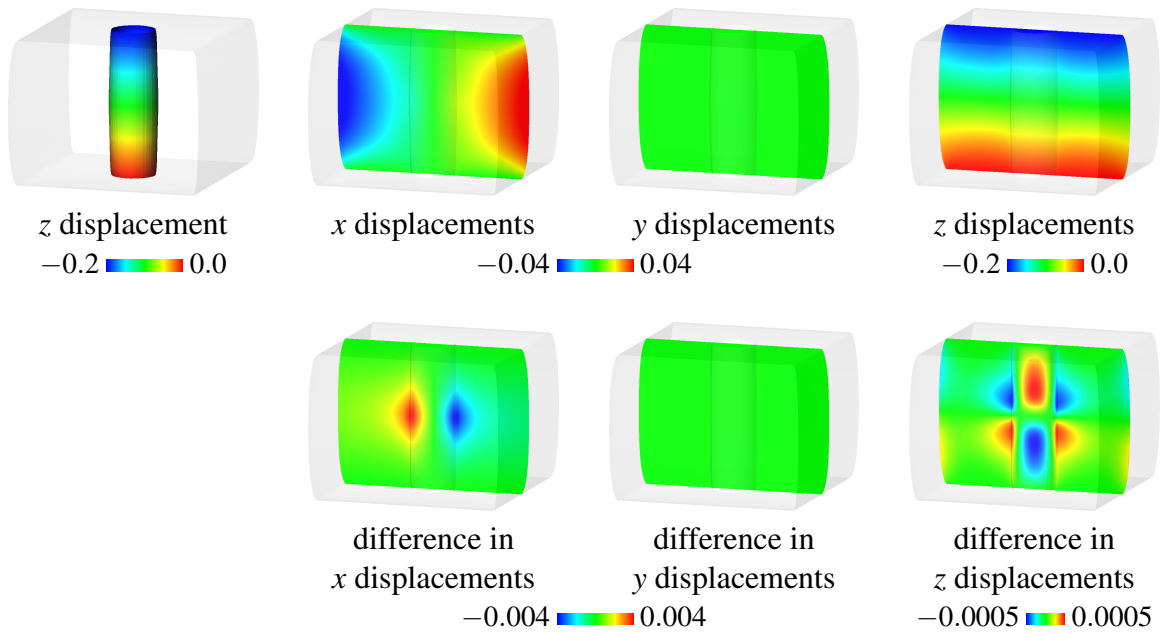


Figure 10: *Top row*: 20 % compression of an embedded column with varying (isotropic—transversely isotropic—) elasticity tensor in the column. From left to right, the images show the deformed configuration with z displacements on the interface between column and embedding and displacements in the three space directions on a slice through the center of the combined object. *Bottom row*: For comparison, we show the differences to displacements obtained for a constant isotropic tensor throughout the column.

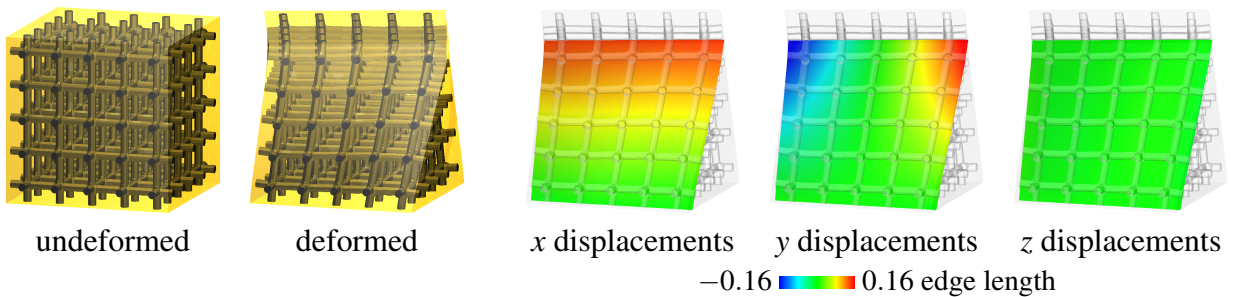


Figure 11: Torsion of an artificial trabecular dataset with varying transverse isotropy embedded in softer isotropic material. Displacements in the three space directions are shown in a slice near the front of the sample.

Acknowledgments

Ole Schwen was supported by the DFG project RU567/8-2 “Multiscale Simulation and Validation of the Elastic Microstructures of Vertebral Bodies”. The authors would like to thank Hans-Joachim Wilke and Uwe Wolfram for the datasets used in the simulations shown in Figures 6 and 8. We are grateful to Stefan Sauter for his advice on composite finite elements and to Benedikt Wirth for extensive discussions on the construction of the elasticity interpolation scheme.

References

- [1] T. Belytschko, Y. Krongauz, D. Organ, M. Fleming, and P. Krysl, *Meshless methods: An overview and recent developments*, Computer methods in applied mechanics and engineering **139** (1996), 3–47.
- [2] Marshall Bern and David Eppstein, *Computing in Euclidian geometry*, Lecture Notes Series on Computing, vol. 1, ch. Mesh generation and optimal triangulation, pp. 23–90, World Scientific, Singapore, 1992.
- [3] Steven K. Boyd and Ralph Müller, *Smooth surface meshing for automated finite element model generation from 3D image data*, Journal of Biomechanics **39** (2006), no. 7, 1287–1295.
- [4] Achi Brandt, *Multi-level adaptive solutions to boundary-value problems*, Mathematics of Computation **31** (1977), no. 138, 333–390.
- [5] Yan Chevalier, Dieter Pahr, Helga Allmer, Mathieu Charlebois, and Philippe Zysset, *Validation of a voxel-based FE method for prediction of the uniaxial apparent modulus of human trabecular bone using macroscopic mechanical tests and nanoindentation*, Journal of Biomechanics **40** (2007), 3333–3340.
- [6] C. Armando Duarte, *A review of some meshless methods to solve partial differential equations*, TICAM Report 95-06, Texas Institute for Computational and Applied Mathematics, University of Texas at Austin, U.S.A., 1995.
- [7] Iain S. Duff and Gérard A. Meurant, *The effect of ordering on preconditioning conjugate gradients*, BIT Numerical Mathematics **29** (1989), 635–657.
- [8] Thomas-Peter Fries and Hermann-Georg Matthies, *Classification and overview of meshfree methods*, Informatikbericht 2003-3, Institute of Scientific Computing, Technical University Braunschweig, 2004, (revised version).
- [9] T. Gao, W. H. Zhang, J. H. Zhu, Y. J. Xu, and D. H. Bassir, *Topology optimization of heat conduction problem involving design-dependent heat load effect*, Finite Elements in Analysis and Design **44** (2008), no. 14, 805–813.
- [10] N. A. Golias and T. D. Tsiboukis, *An approach to refining three-dimensional tetrahedral meshes based on Delaunay transformations*, International Journal for Numerical Methods in Engineering **37** (1994), 793–812.
- [11] T. Grauschopf, M. Griebel, and H. Regler, *Additive multilevel preconditioners based on bilinear interpolation, matrix-dependent geometric coarsening and algebraic multigrid coarsening for second-order elliptic PDEs*, Applied Numerical Mathematics **23** (1997), no. 1, 63–95.
- [12] Ramesh M. Gulrajani, *The forward and inverse problems of electrocardiography*, IEEE Engineering in Medicine and Biology **17** (1998), no. 5, 84–101.
- [13] Wolfgang Hackbusch, *Iterative solution of large sparse systems of equations*, Applied Mathematical Sciences, vol. 95, Springer, 1994.

- [14] V. Kosmopoulos and T. S. Keller, *Damage-based finite-element vertebroplasty simulations*, *European Spine Journal* **13** (2004), 617–625.
- [15] Tim Kröger, Inga Altrogge, Tobias Preusser, Philippe L. Pereira, Diethard Schmidt, Andreas Weihusen, and Heinz-Otto Peitgen, *Numerical simulation of radio frequency ablation with state dependent material parameters in three space dimensions*, *Medical Image Computing and Computer-Assisted Intervention – MICCAI 2006* (R. Larsen, M. Nielsen, and J. Sporring, eds.), *Lecture Notes in Computer Science*, vol. 4191, Springer, 2006, pp. 380–388.
- [16] Shaofan Li and Wing Kam Liu, *Meshfree and particle methods and their application*, *Applied Mechanics Reviews* **55** (2002), no. 1, 1–34.
- [17] Florian Liehr, Tobias Preusser, Martin Rumpf, Stefan Sauter, and Lars Ole Schwen, *Composite finite elements for 3D image based computing*, *Computing and Visualization in Science* **12** (2009), no. 4, 171–188.
- [18] William E. Lorensen and Hovey E. Cline, *Marching cubes: A high resolution 3D surface construction algorithm*, *Computer Graphics* **21** (1987), no. 4, 163.
- [19] Elsie F. Morgan, Oscar C. Yeh, and Tony M. Keaveny, *Damage in trabecular bone at small strains*, *European Journal of Morphology* **42** (2005), no. 1/2, 13–21.
- [20] Ralph Müller, Tor Hildebrand, and Ralph Rügsegger, *Non-invasive bone biopsy: a new method to analyse and display the three-dimensional structure of trabecular bone*, *Physics in Medicine and Biology* **39** (1994), no. 1, 145–164.
- [21] Stanley Osher and James A. Sethian, *Fronts propagating with curvature dependent speed: Algorithms based on Hamilton–Jacobi formulations*, *Journal of Computational Physics* **79** (1988), no. 1, 12–49.
- [22] Torben Pätz, *Composite FE für ein Mehrphasen-Modell zur Simulation von Radio-Frequenz-Ablation*, *Diplom thesis*, Universität Bremen, November 2008.
- [23] A. Pegoretti, L. Fambri, G. Zappini, and M. Bianchetti, *Finite element analysis of a glass fibre reinforced composite endodontic post*, *Biomaterials* **23** (2002), no. 13, 2667–2682.
- [24] Tobias Preusser, Martin Rumpf, Stefan Sauter, and Lars Ole Schwen, *3D composite finite elements for elliptic boundary value problems with discontinuous coefficients*, *SIAM Journal on Scientific Computing*, accepted.
- [25] Tobias Preusser, Martin Rumpf, and Lars Ole Schwen, *Finite element simulation of bone microstructures*, *Proceedings of the 14th Workshop on the Finite Element Method in Biomedical Engineering, Biomechanics and Related Fields*, University of Ulm, July 2007, pp. 52–66.
- [26] S. A. Sauter and R. Warnke, *Composite finite elements for elliptic boundary value problems with discontinuous coefficients*, *Computing* **77** (2006), 29–55.
- [27] Lars Ole Schwen, Uwe Wolfram, Hans-Joachim Wilke, and Martin Rumpf, *Determining effective elasticity parameters of microstructured materials*, *Proceedings of the 15th Workshop on the Finite Element Method in Biomedical Engineering, Biomechanics and Related Fields*, University of Ulm, July 2008, pp. 41–62.
- [28] Jonathan Richard Shewchuk, *Lecture notes on Delaunay mesh generation*, 1999.
- [29] _____, *What is a good linear element? Interpolation, conditioning, and quality measures*, *Proceedings of the 11th International Meshing Roundtable*, Sandia National Laboratories, September 2002, pp. 115–126.

- [30] Shang-Hua Teng and Chi Wai Wong, *Unstructured mesh generation: Theory, practice and applications*, International Journal of Computational Geometry & Applications **10** (2000), no. 3, 227–266.
- [31] P. J. Thurner, P. Wyss, R. Voide, M. Stauber, M. Stampanoni, U. Sennhauser, and R. Müller, *Time-lapsed investigation of three-dimensional failure and damage accumulation in trabecular bone using synchrotron light*, Bone **39** (2006), 289–299.
- [32] G. M. Treece, R. W. Prager, and A. H. Gee, *Regularized marching tetrahedra: improved iso-surface extraction*, Computers and Graphics **23** (1999), no. 4, 583–598.
- [33] B. van Rietbergen, R. Huiskes, F. Eckstein, and P. Ruegsegger, *Trabecular bone tissue strains in the healthy and osteoporotic human femur*, Journal of Bone and Mineral Research **18** (2003), no. 10, 1781–1788.
- [34] W. Voigt, *Ueber die Beziehung zwischen den beiden Elasticitätsconstanten isotroper Körper*, Annalen der Physik **274** (1889), no. 12, 573–587.
- [35] Adam Wittek, Ron Kikinis, Simon K. Warfield, and Karol Miller, *Brain shift computation using a fully nonlinear biomechanical model*, Medical Image Computing and Computer-Assisted Intervention – MICCAI 2005 (J. Duncan and G. Gerig, eds.), Lecture Notes in Computer Science, vol. 3750, Springer, 2005, pp. 583–590.
- [36] Uwe Wolfram, Hans-Joachim Wilke, and Philippe K. Zysset, *Transverse isotropic elastic properties of vertebral trabecular bone matrix measured using microindentation under dry conditions (effects of age, gender and vertebral level)*, Journal of Mechanics in Medicine and Biology, accepted.
- [37] Dae Gon Woo, Ye-Yeon Won, Han Sung Kim, and Dohyung Lim, *A biomechanical study of osteoporotic vertebral trabecular bone: The use of micro-CT and high-resolution finite element analysis*, Journal of Mechanical Science and Technology **21** (2007), 593–601.
- [38] Jinchao Xu, *Theory of multilevel methods*, PhD dissertation, Cornell University, May 1989.
- [39] _____, *Iterative methods by space decomposition and subspace correction*, SIAM Review **34** (1992), no. 4, 581–613.